RSC Advances

PAPER

View Article Online
View Journal | View Issue

Cite this: *RSC Adv.*, 2019, **9**, 33486

Fabrication of a low-cost adsorbent supported zero-valent iron by using red mud for removing Pb(II) and Cr(VI) from aqueous solutions

Yufeng Du,[a] Min Dai,[b] Jiangfei Cao[b] and Changsheng Peng *[ab]

In this study, a granular red mud supported zero-valent iron (ZVI@GRM) was successfully prepared and was used to remove Pb(II) and Cr(VI) from aqueous solution. Zero-valent iron (ZVI) was synthesized by direct reduction of iron oxide in red mud by maize straw as a reductant at 900 °C in an anoxic atmosphere. The technical characterization (SEM, EDS, XRD, FTIR and BET) revealed that ZVI@GRM was loaded with zero-valent iron and contained different size pores. The factors of adsorption experiments include initial concentration, contact time, pH and temperature. The Pb(II) and Cr(VI) removal by ZVI@GRM well fitted the pseudo-second-order kinetics model and the removal of heavy metals was an endothermic process. Essentially, Pb(II) was transformed to precipitate forms (Pb^0, $Pb(OH)_2$, or $2PbCO_3 \cdot Pb(OH)_2$) and Cr(VI) was converted to $Cr(OH)_3$ or Cr^{3+}/Fe^{3+} hydroxides. The maximum removal capacity for Pb(II) and Cr(VI) by ZVI@GRM was 149.42 and 37.14 mg g^{-1}. ZVI@GRM was a low-cost material and had outstanding performance and great potential in wastewater treatment.

Received 2nd September 2019
Accepted 8th October 2019

DOI: 10.1039/c9ra06978j

rsc.li/rsc-advances

1. Introduction

Red mud (bauxite residue) is produced by adding concentrated caustic soda to the alumina production process to dissolve the bauxite. The volume of red mud generated per ton of alumina product is approximately 0.5–2 tons.[1,2] The large demand for alumina has increased the rate of red mud production. Globally, the cumulative stock of red mud exceeds 4 billion tons and is still growing rapidly.[3–5] At present, stockpiling and ocean disposal are the main disposal methods of red mud; only a small amount is utilized for building materials,[6,7] land composting,[8] metal recovery[9,10] and environmental restoration materials.[11,12] The inappropriate disposal of red mud not only increases economic cost, but also causes environmental pollution problems. Thus, this is an urgent problem for the alumina industry.

In the past years, researchers have shown much interest in the use of red mud as an adsorbent for removing pollutants, such as phosphate,[13] arsenate,[14] fluoride,[15] dyes[16] and heavy metals,[17] from aqueous solution. However, these studies primarily have focused on the use of powdered red mud because of the nature of its composition and structure. The powder red mud has a relatively large adsorption capacity, due to the high specific surface area and it has the disadvantage of in practical wastewater treatment applications including difficult to regenerate and recover after the application. Therefore, it is necessary to prepare a convenient and low-cost granular red mud adsorbent used in aqueous solutions.

The mineral composition of red mud includes various forms of iron, aluminum oxides and aluminosilicates. Researchers have focused on the red mud reuse for the recovery of metals, which transforms the waste into more valuable resource.[18,19] Iron oxide as the major constituent is about 35–55% in the red mud depending on the bauxite characteristics.[20,21] Recovery of iron from red mud has been a matter of research for many years. Carbothermic reduction is mainly used to convert Fe_2O_3 into Fe_3O_4 and separate by magnetic separation.[9,22] However, few researchers have conducted in the reduction of iron oxide in red mud to Fe^0 (zero valent iron, ZVI) by carbothermic method and application in water treatment. Recently, ZVI has attracted much attention and has been widely used in the field of water treatment due to its high reduction capacity, larger surface area and environment friendly.[23,24] At present, ZVI is mainly produced by the reaction of $NaBH_4/KBH_4$ with Fe^{2+}/Fe^{3+}, but the $NaBH_4/KBH_4$ is expensive and ZVI particles tend to aggregate and oxidize in aqueous solution, resulting in a decrease in catalytic ability and limiting the application of water treatment. The carbothermic can convert the Fe_2O_3 in the granular red mud to ZVI and embed it in the material to reduce the agglomeration of ZVI, and this is a low-cost way to solve the disadvantages of powdered red mud and ZVI in wastewater treatment.

In this work, a novel and low-cost method was used to prepare ZVI, which was directly synthesized by direct reduction of iron oxide in red mud at 900 °C in anoxic atmosphere. ZVI

[a]*The Key Lab of Marine Environmental Science and Ecology, Ministry of Education, Ocean University of China, Qingdao 266100, China. E-mail: pcs005@ouc.edu.cn*
[b]*School of Environmental and Chemical Engineering, Zhaoqing University, Zhaoqing, 526061, China*

was well distributed in porous adsorption materials. Red mud was used as the main raw material to prepare the granular red mud adsorbents (ZVI@GRM), bentonite and maize straw were applied as binding agent and pore producer. Then the granular red mud adsorbent supported ZVI was used for removal Pb(II) and Cr(VI) in aqueous solutions.

2. Experiment

2.1. Materials

Red mud (RM) was obtained from the Shandong Aluminum Industry Co. Ltd. (Zibo, China). Bentonite was obtained from the Shandong Huawei Bentonite Co. Ltd. (Qingdao, China). Maize straw was collected from farmland (Qingdao, China). The chemical composition of RM and bentonite was analyzed through X-ray Fluorescence Spectrometer (XRF, Axios-pw4400) is shown in Table 1, indicating that RM and bentonite are primarily a mixture of Fe, Al, Si and oxides. All the chemicals used in this study were analytical grade, including potassium dichromate ($K_2Cr_2O_7$), lead nitrate (Pb $(NO_3)_2$), hydrochloric acid (HCl), sodium hydroxide (NaOH), ferric chloride hexahydrate ($FeCl_3 \cdot 6H_2O$), phosphoric acid (H_3PO_4) was purchased from Tianjin Chemical Reagent Co., Ltd. (Tianjin, China). Distilled water was used in all preparations. The solution pH was adjusted by using HCl and NaOH solutions.

2.2. Preparation of ZVI@GRM

The schematic diagram of ZVI@GRM preparation is shown in Fig. 1. ZVI@GRM was made by using raw materials with RM (red mud), maize straw and bentonite. The RM and bentonite were dried at 85 °C for 24 h and sieved through a 100 mesh. Maize straw was cut into small pieces and washed clearly with distilled water. After being dried at 85 °C for 24 h, the pieces were comminuted with a micro plant grinding machine and sieved through a 100 mesh. Then the granular adsorbent was prepared at a mass ratio of 2 : 1 : 0.5 (RM : Maize straw : Bentonite), adding distilled water to the blender until it could be molded. The mixture was extruded through an aperture board to get cylindrical particles with the diameter of 4 mm and the particles were dried at 105 °C until it reached constant weight. The particles were called GRM (granular red mud). And then, they were sintered in an atmosphere sintering furnace at 900 °C with the heating rate 10 °C min^{-1} under anoxic atmosphere. After naturally cooling down in a vacuum, and stored in a vacuum desiccator to avoid being oxidized, ZVI@GRM was finally obtained.

2.3. Characterization

The morphological analysis of GRM and ZVI@GRM were performed using a scanning electron microscopy (SEM, JSM-6700F). The elemental compositions were determined by energy dispersive spectroscopy (EDS, JSM-6700F). The BET-N_2 adsorption method was used to test the specific surface area with a surface analyzer (Micromeritics, ASAP 2020). The X-ray Diffraction (XRD) patterns was determined by XRD (D/max-γB). The functional groups were identified using Fourier transform infrared spectroscopy (FTIR, Bruker Vertex 70).

Table 1 The composition of RM (wt%)

Raw materials	Fe_2O_3	Al_2O_3	SiO_2	Na_2O	TiO_2	CaO	K_2O
RM	35.6	23.4	16.2	13.4	6.6	3.3	0.07

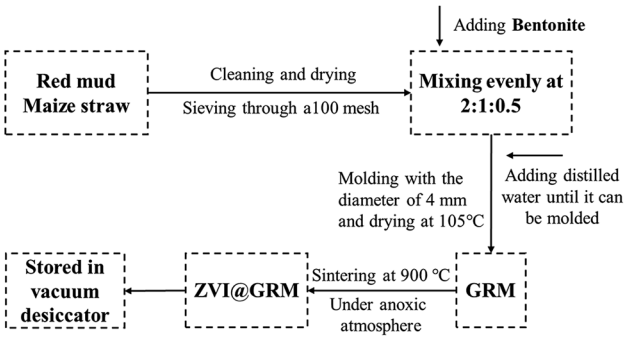

Fig. 1 Scheme of the procedure for ZVI@GRM preparation.

2.4. Adsorption experiments

The solutions of Pb(II) and Cr(VI) (1000 mg L^{-1}) were prepared by dissolving 1.5990 g of Pb $(NO_3)_2$ and 2.8289 g of $K_2Cr_2O_7$. All the batch experiments were conducted in 250 mL conical flasks containing 100 mL of Pb(II) and Cr(VI) solution at 120 rpm in a shaker and a series of removal experiments were conducted in duplicate by using ZVI@GRM. The initial pH of Pb(II) in a range of 1.0 to 7.0 and Cr(VI) in a range of 1.0 to 13.0 was studied. The pH was adjusted with 0.1 mol L^{-1} NaOH or 0.1 mol L^{-1} HCl solutions. The initial concentration of Pb(II) (100, 200, 400 mg L^{-1}) and Cr(VI) (20, 50, 100 mg L^{-1}) was studied. The temperature (298.15, 308.15, 318.15 K) on the removal of Pb(II) and Cr(VI) by ZVI@GRM was studied. The concentration of Pb(II) in solutions was measured using an atomic adsorption spectrophotometer (AAS). The concentration of Cr(VI) was determined by the 1,5-diphenylcarbazide method at a wavelength of 540 nm on UV-vis spectrophotometer. The removal amount and efficiency of Pb(II) and Cr(VI) were calculated by the following formula:

$$q_t = \frac{(C_0 - C_t) \times V}{w} \quad (1)$$

where q_t (mg g^{-1}) is the removal capacity of Pb(II) and Cr(VI), C_0 (mg L^{-1}) is the initial concentration of Pb(II) and Cr(VI), C_t (mg L^{-1}) is the concentration of Pb(II) and Cr(VI) at time t, w (g) is the weight of the adsorbent, V (L) is the volume of solutions.

3. Results and discussion

3.1. Characterizations

3.1.1 SEM and EDS. The Fig. 2 shows the SEM images of GRM, ZVI@GRM and after Pb(II) and Cr(VI) removal, and the elemental mapping images of ZVI@GRM and after Pb(II) and Cr(VI) removal. It can be seen clearly that the particle surface is

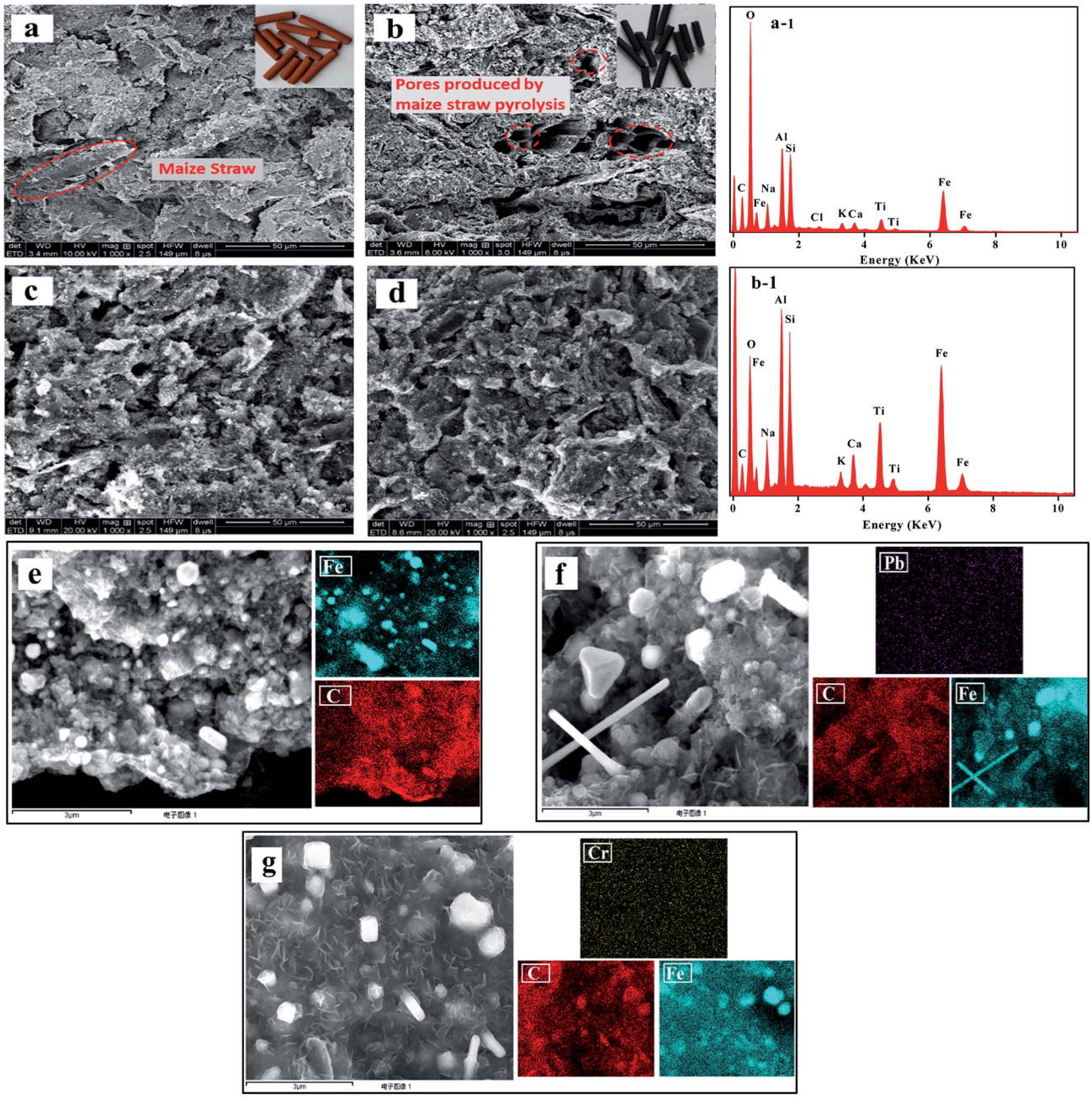

Fig. 2 SEM image of GRM (a), ZVI@GRM (b), ZVI@GRM after Pb(II) removal (c) and Cr(VI) removal (d); EDS image of GRM (a-1) and ZVI@GRM (b-1); Elemental mapping images of ZVI@GRM (e), ZVI@GRM-Pb (f) and ZVI@GRM-Cr (g).

tight and a part of the fibrous maize straw exited in GRM from Fig. 2a. However, plenty of produced pores appeared in ZVI@GRM after sintering. These pores were produced by organic substances in the maize straw during the pyrolysis process (Fig. 2b). In addition, the fibrous maize straw could be connected to the pores during the pyrolysis process, increasing the specific surface area of adsorbent.[25] This also proved that porous adsorbent. Under anoxic atmosphere, the biochar produced by maize straw as a carbon source for reducing zero valent iron. The ZVI formed by solid phase reduction can distribute evenly on the carrier without clustering phenomenon. The elements of GRM and ZVI@GRM are shown in Fig. 2(a-1 and b-1). It was proved that ZVI@GRM was mainly composed of Fe, O, Al, Si, and C. Compared to GRM, the decrease of C and O in ZVI@GRM after sintering was mainly due to pyrolysis of organic and decomposition of carbonate and the reduction of combined water. The elemental mapping of ZVI@GRM in Fig. 2e shows that Fe and C are evenly distributed on the surface of the material. Moreover, after adsorbing Pb(II) and Cr(VI), the surface of the material becomes rough and without obvious pore structure, probably because Pb(II) and Cr(VI) were adsorbed and precipitates formed on the surface and

inside of the material (Fig. 2c and d). The elemental mapping of ZVI@GRM after Pb(II) and Cr(VI) removal proves that the existence of Pb and Cr on the surface (Fig. 2f and g). This indicates that Pb and Cr were adsorbed on ZVI@GRM.

3.1.2 XRD. The XRD patterns of GRM and ZVI@GRM are shown in Fig. 3a. The XRD patterns shown that the mineral composition of red mud was more complicated. The typical peak of ZVI (2θ at 44.64°, 65.166°) confirmed its existence in prepared ZVI@GRM and the peak of Fe_2O_3 (2θ at 35.68° and 35.45°) decreased.[26] Meanwhile, this also confirmed that iron oxide was reduced to ZVI by solid phase reduction at 900 °C. After sintering, the peak of AlOOH, Al $(OH)_3$ and $CaCO_3$ disappeared while the peak of $Ca_3Al_2O_6$, Ca_2SiO_4, $Ca_3Fe_2Si_3O_{12}$ and Al_2O_3 begin to appear. As the formation of $Ca_3Al_2O_6$ by CaO and Al_2O_3, were speculated to result in the ZVI@GRM strength enhancing.[27] Accordingly, the main reactions that occurred during the sintering process could be described as follows:

$$C + CO_2 \rightarrow 2CO \quad (2)$$

$$Fe_2O_3 + 3CO \rightarrow 2Fe + 3CO_2 \quad (3)$$

$$CaCO_3 \rightarrow CaO + CO_2 \quad (4)$$

$$Al(OH)_3 \rightarrow 2AlOOH + 2H_2O \quad (5)$$

$$2AlOOH \rightarrow Al_2O_3 + H_2O \quad (6)$$

$$3CaO + Al_2O_3 \rightarrow Ca_3Al_2O_6 \quad (7)$$

$$3CaO + Fe_2O_3 + 3SiO_2 \rightarrow Ca_3Fe_2Si_3O_{12} \quad (8)$$

$$2CaO + SiO_2 \rightarrow Ca_2SiO_4 \quad (9)$$

In summary, the ZVI@GRM was an adsorbent material rich in zero-valent iron, which based on Fe–Al–Si–Ca related compounds with high strength and adsorption activity.

3.1.3 FTIR. The FTIR spectra in the range of 400 to 4000 cm^{-1} of GRM and ZVI@GRM are presented in Fig. 3b. The two peaks at around 3415 cm^{-1} (O–H stretching vibration) and 1637 cm^{-1} (O–H bending vibration) were assigned to the vibration of hydroxyl groups and were likely due to the presence of H_2O or hydroxyl compounds in GRM and ZVI@GRM.[28] Meanwhile, the peak at 2922 cm^{-1} indicated the presence of $-CH_2$ stretching of aliphatic compound, it was dismissed during the sintering progress due to the decomposition of organics at high temperature.[29] The peak at 1419 cm^{-1} represented –COOH stretching vibration. The characteristic band at 1002 cm^{-1} corresponded to Si–O–Si in silicate groups.[30] The peak at 703 cm^{-1} corresponded to Al–O band and became more distinct after sintering because of the band of Al–O was tighter at high temperature.[31] Furthermore, the peaks at 468 cm^{-1} and 521 cm^{-1} were observed on Fe–O of Fe_2O_3 and Fe_3O_4, indicating that Fe compounds existed in the adsorbents.[32] These results and XRD analysis demonstrated that ZVI could be successfully loaded onto the surface of ZVI@GRM.

3.1.4 BET. The BET analysis of ZVI@GRM is shown in Fig. 4. According to the IUPAC classification, the nitrogen adsorption–desorption isotherms of ZVI@GRM belongs to a typical type IV with a type H1 hysteresis loop due to the mesoporous pores of ZVI@GRM (Fig. 4a). As shown in Fig. 4b the pore size distribution curve of ZVI@GRM indicated that the pores in the sample are mainly mesopores (2–50 nm), and a small number of micropores and macropores. According to the results, the specific surface area and average pore size were 44.575 $m^2\ g^{-1}$ and 3.413 nm, respectively.

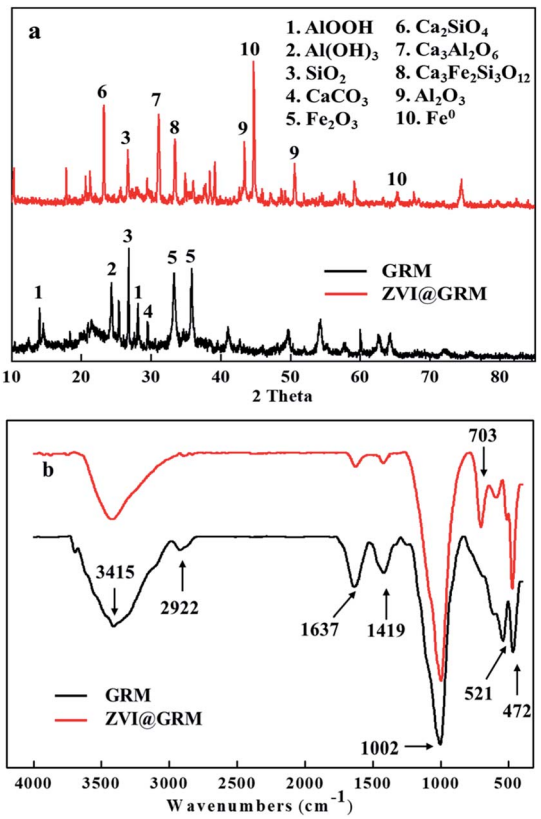

Fig. 3 XRD pattern (a); FTIR spectra (b) of GRM and ZVI@GRM.

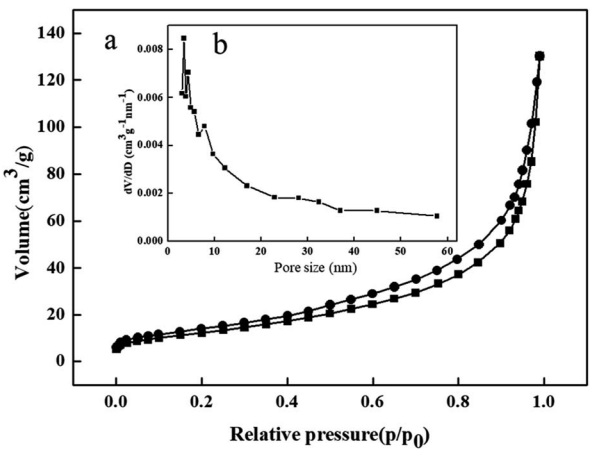

Fig. 4 (a) Nitrogen adsorption–desorption isotherm of ZVI@GRM; (b) pore size distribution of ZVI@GRM.

3.2 Effect of initial pH on Pb(II) and Cr(VI) removal

The initial pH of solution is considered as a significant influence on the adsorption process. This is mainly due to the solution pH affects the surface charges of adsorbents and the speciation of lead and chromium ions in aqueous solution. The effect of initial pH of removal of Pb(II) and Cr(VI) from solution is shown in Fig. 5. The result indicated that the removal amount of Cr(VI) decreased with the increased pH from 1.0 to 13.0 and the removal amount of Pb(II) increased with the increased pH from 1.0 to 7.0. In the solution, Pb existed in the form of Pb(II) and Cr has two forms of Cr(VI), the $HCrO_4^-$ was in solution at pH < 6.0 and the CrO_4^{2-} in solution at pH > 6.0.[33] At low pH, the competition for a vacant adsorbent site between the high concentration of H^+ and Pb(II), inhibiting the removal of Pb(II). Thus, the Pb(II) could not smoothly move toward the positively charged surface of ZVI@GRM due to electrostatic repulsion and significantly affected Pb(II) adsorption at low pH. On the contrary, it was benefits for Cr(VI) removal that the electrostatic repulsive force between ZVI@GRM and $HCrO_4^-$ reduced at lower pH.[34,35]

In Fe^0 treatment systems, the Cr(VI) and Pb(II) removal mechanism was generally considered to the electron transfer take place on the surface from Fe^0 and it was oxidized to Fe^{2+}/Fe^{3+} with the reduction of Pb(II) to Pb^0 and Cr(VI) to Cr(III) under acidic conditions.[36] As the pH_{pzc} of ZVI@GRM was 5.2 determined by measuring the zeta potential of the solution at different pH. When pH > 5, the electrostatic attraction between ZVI@GRM and Pb(II) accelerated the adsorption progress and the high concentration of OH^- reacted with Pb(II) to form Pb$(OH)_2$ precipitation,[37] resulting a decrease in the Pb(II) concentration in the solution.

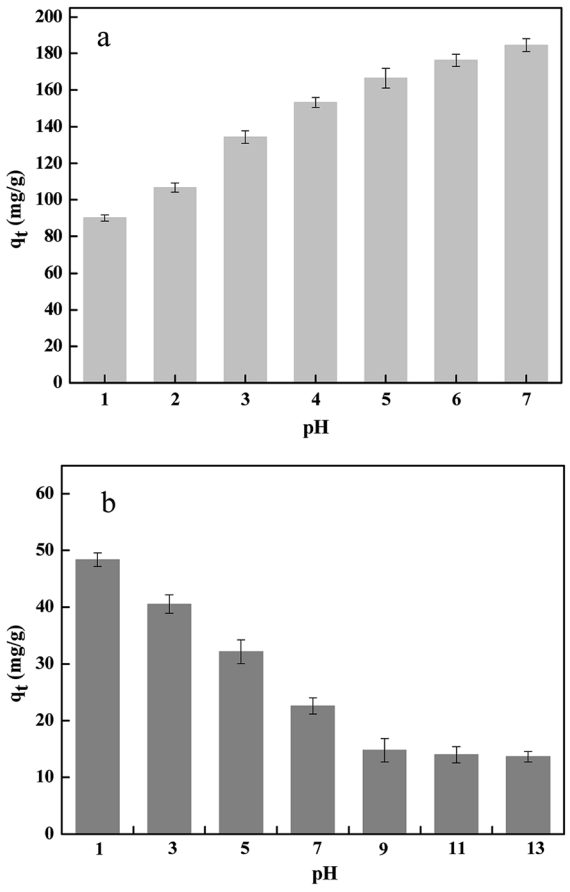

Fig. 5 The effect of initial pH on Pb(II) (a) and Cr(VI) (b) removal amount.

3.3 Effect of initial concentration and sorption kinetics

The pseudo-first-order and pseudo-second-order adsorption kinetics models used for describing the adsorption of Pb(II) and Cr(VI) on GRM@ZV which involves adsorption and chemical reduction. The kinetics equations are as follows:

Pseudo-first-order kinetics model:

$$\ln(q_e - q_t) = \ln q_e - k_1 t \quad (10)$$

Pseudo-second-order kinetics model:

$$\frac{t}{q_t} = \frac{1}{k_2 q_e^2} + \frac{t}{q_e} \quad (11)$$

where q_e and q_t (mg g^{-1}) are the adsorption amounts of CV adsorbed on the adsorbent at equilibrium and at different times t. k_1 and k_2 are the rate constant of first and second order kinetic models in h^{-1} and g (mg^{-1} h), respectively.

In this study, the adsorption of Pb(II) and Cr(VI) on ZVI@GRM were conducted at 298.15 K and initial concentrations of 100, 200, 400 mg L^{-1} and 20, 50, 100 mg L^{-1}. The calculated kinetic parameters in Table 2 are shown that the correlation coefficient (R^2) was low when the data was fitted with the pseudo-first-order model. In comparison, the pseudo-second order model was more suitable for data fitting ($R^2 > 0.99$). Plots of q_t *versus* t and t/q_t *versus* t of Pb(II) and Cr(VI) are shown in Fig. 6. Fig. 6(a and b) shows that the effect of initial Pb(II) and Cr(VI) concentration on removal amount. Obviously, the removal rate of Pb(II) and Cr(VI) were high at initial adsorption progress due to most adsorption sites and the large surface area of ZVI@GRM and it was good for the adsorption of heavy metal.[38,39] As the initial concentration of Pb(II) and Cr(VI) increased, the concentration difference between the surface layer of ZVI@GRM and the adsorbate enhanced, so the driving force of ions diffusing to the adsorption surface increased, resulting in the high removal amount. Nevertheless, under the same conditions, the Pb removal amount by ZVI@GRM was higher than Cr at the different initial concentrations. This could be explained by that Pb(II) with positive charged may be more easily absorbed onto the surface of ZVI@GRM than negative charged $HCrO_4^-$/CrO_4^{2-}. In addition, the Pb(II) radius is smaller than $HCrO_4^-$/CrO_4^{2-} and more easily adsorbed by ZVI@GRM. Furthermore, red mud contains a large amount of metal oxides, which leads to hydroxyl and carboxyl groups on the ZVI@GRM surface.[40,41]

The curves of fitted pseudo-second-order adsorption kinetics on Pb(II) and Cr(VI) are shown in Fig. 6(c and d). The experimental data well fit with the pseudo-second-order kinetic model indicated that the removal process of Pb(II) and Cr(VI) on ZVI@GRM was dominated by chemical interaction and removal rates were controlled by the adsorption process.

Table 2 Corresponding parameters of kinetics models

Concentration (mg L^{-1})		Pseudo-first-order model			Pseudo-second-order model		
		q_e, mg g^{-1}	k_1, h^{-1}	R^2	q_e, mg g^{-1}	k_2, g (mg h)$^{-1}$	R^2
Pb	100	52.24	0.0677	0.9772	82.64	0.0024	0.9996
	200	82.92	0.0696	0.9729	131.58	0.0013	0.9966
	400	86.27	0.0702	0.9556	181.82	0.0011	0.9963
Cr	20	10.05	0.0516	0.9493	16.13	0.011	0.9992
	50	11.7	0.05	0.9109	34.13	0.0044	0.9989
	100	17.8	0.0602	0.9281	38.31	0.0094	0.9993

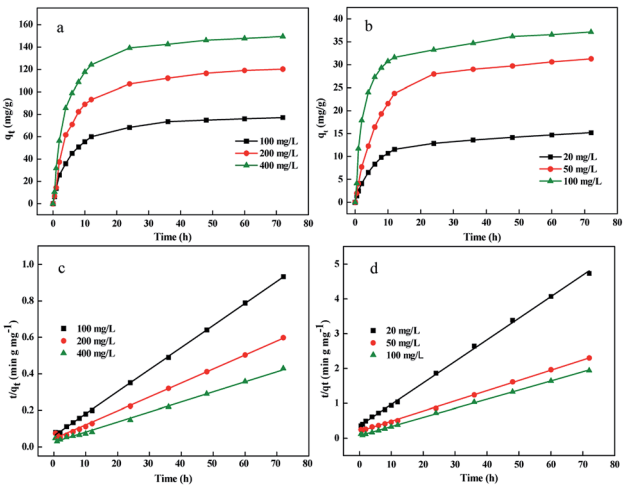

Fig. 6 The effect of initial concentration of Pb(II) (a) and Cr(VI) (b) removal amount and curves of fitted pseudo-second-order adsorption kinetics on Pb(II) (c) and Cr(VI) (d).

3.4 Effect of contact temperature and sorption isotherms

The Langmuir model proposed that the adsorption progress on a solid surface occurs in a monolayer and the adsorption sites are of equivalent energy. The equation can be described as:

$$\frac{C_e}{q_e} = \frac{1}{bq_m} + \frac{C_e}{q_m} \quad (12)$$

where C_e (mg L^{-1}) is the equilibrium concentration of Pb(II) and Cr(VI), q_e (mg g^{-1}) is the adsorption amount at equilibrium (mg g^{-1}), q_m (mg g^{-1}) is the maximum adsorption capacity and b (L mg^{-1}) is the Langmuir constant.

On the contrary, the Freundlich isotherm is described as assuming that the adsorption occurs on a heterogeneous surface and non-uniform distribution of the adsorption heat over the adsorbent surface takes place.[42] This can be expressed by:

$$\log q_e = \log K_f + \frac{1}{n}\log C_e \quad (13)$$

where C_e (mg L^{-1}) is the equilibrium concentration of Pb(II) and Cr(VI), q_e (mg g^{-1}) is the equilibrium adsorption amount (mg g^{-1}). Where K_f and n are constants related to the adsorbent capacity and the adsorption intensity, respectively. K_f and n values can be calculated from the plot of ln q_e *versus* ln C_e.

The relevant parameters of Pb(II) and Cr(VI) adsorption isotherm adsorbed on GRM@ZVI are shown in Table 3. The results show that the correlation coefficient R^2 of Langmuir models ($R^2 > 0.99$) was higher than that of Freundlich models. The maximum adsorption q_m (188.67 and 51.55 mg g^{-1}) of Pb(II) and Cr(VI) calculated by Langmuir model was close to the actual equilibrium adsorption (181.52 and 50.16 mg g^{-1}). In addition, Fig. 7 shows the sorption isotherms of Pb(II) and Cr(VI) at different temperature by plotting C_0 *versus* q_t. The figures were consistent with the constant partition ("*C*") type sorption isotherms resulting that the original sites were replaced by new sorption sites formed on the ZVI@GRM surface.[43] The new sorption sites were due to the aging of the surface, such as the new OH^- formation by the interactions between ZVI@GRM and H_2O. Besides, the Fig. 7 also shows that Pb(II) and Cr(VI) removal amount increases with the increased temperature, suggesting that removal was an endothermic process. This result can be further explained by adsorption thermodynamic study.

Table 3 Corresponding parameters of Langmuir and Freundlich models

Temperature (K)		Langmuir			Freundlich		
		q_e, mg g^{-1}	k_1, h^{-1}	R^2	K_f	n	R^2
Pb	298.15	188.67	0.0205	0.9976	36.87	3.95	0.9704
	308.15	204.08	0.0289	0.9990	49.92	4.64	0.9641
	318.15	212.76	0.0389	0.9986	65.31	5.45	0.9886
Cr	298.15	51.55	0.0557	0.9975	12.86	4.18	0.9141
	308.15	54.64	0.0758	0.9978	15.73	4.54	0.8511
	318.15	57.47	0.1438	0.9988	17.98	4.67	0.8495

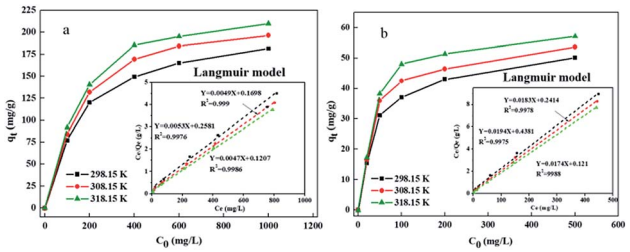

Fig. 7 Sorption isotherms of Pb(II) (a) and Cr(VI) (b) at different temperature.

3.5 Thermodynamic study

The thermodynamic parameters including the enthalpy change (ΔH, kJ mol^{-1}), Gibbs free energy change (ΔG, kJ mol^{-1}), and entropy change (ΔS, J (K^{-1} mol)) for Pb(II) and Cr(VI) removal were calculated by the following equations:[43]

$$K_c = q_e/C_e \quad (14)$$

$$\Delta G = -RT\ln(K_C) = -RT\ln(q_e/C_e) \quad (15)$$

$$\ln(K_c) = \frac{\Delta G}{-RT} = \frac{\Delta H - T\Delta S}{-RT} = -\frac{\Delta H}{RT} + \frac{\Delta S}{R} \quad (16)$$

where K_c is the equilibrium constant, and q_e (mg g^{-1}) and C_e (mg L^{-1}) are the equilibrium adsorption amount on adsorbents and the equilibrium concentrations in the solution, respectively. R is the universal gas constant (8.314 J (K^{-1} mol)). The values of ΔH and ΔS were calculated from the plot of ln K_c *versus* $1/T$.

The values are shown in Table 4 and Fig. 8. In this work, the experiment was conducted under 400 mg L^{-1} (Pb) and 100 mg L^{-1} (Cr) initial concentrations at 298.15 K, 308.15 K and 318.15 K. The ΔG value of Pb(II) and Cr(VI) adsorption were −15.86, −16.69, −17.51 and −15.92, −17.06, −18.19 kJ mol^{-1}, respectively, implying that the adsorption progress was spontaneous.[44] In addition, the decreased values of ΔG with the temperature from 298.15 K to 318.15 K were conducive to the adsorption of Pb(II) and Cr(VI). The $\Delta H > 0$ indicated that the adsorption process was an endothermic reaction under natural conditions, and the adsorption amount increased with increasing temperature, which were consistent with the isotherms study results.[45] The positive ΔS value indicated that the disorder degree of the solid–liquid system composed with the ZVI@GRM and solution increased which was the spontaneous reaction process of entropy increase.

Table 4 Thermodynamic parameters for Pb(II) and Cr(VI) removal by ZVI@GRM at different temperature

	Temperature, K	ΔH, kJ mol^{-1}	ΔS, J (K mol)$^{-1}$	ΔG, kJ mol^{-1}
Pb	298.15	8.77	82.6	−15.86
	308.15	8.77	82.6	−16.69
	318.15	8.77	82.6	−17.51
Cr	298.15	17.89	113.42	−15.92
	308.15	17.89	113.42	−17.06
	318.15	17.89	113.42	−18.19

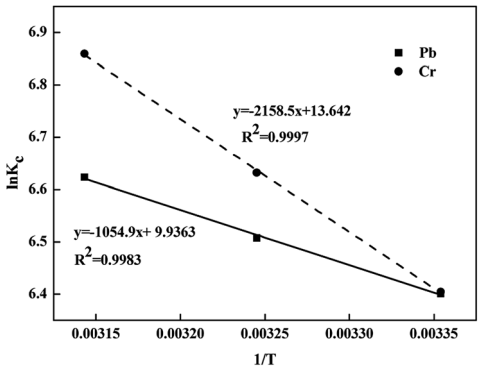

Fig. 8 Plot of ln K_c *versus* $1/T$ for determination of Pb(II) and Cr(VI) removal reaction enthalpy.

3.6 Comparison of different adsorbents for Pb(II) and Cr(VI) removal

Table 5 summarized the maximum removal capacity of different adsorbents for Pb(II) and Cr(VI) removal. As shown in Table 5, the maximum removal capacity of ZVI@GRM for Pb(II) and Cr(VI) was 188.67 and 51.55 mg g^{-1} and it was higher than other analogous adsorbents. In addition, the ZVI@GRM is quite a low-cost material made from red mud, bentonite and straw as raw materials. Thus, ZVI@GRM has important potential in heavy metal wastewater treatment industry.

3.7 Removal mechanisms

The Pb(II) and Cr(VI) removal by ZVI@GRM involved multiple processes such as adsorption, redox reaction, galvanic interactions and precipitation. The removal mechanism in aqueous solution was summarized by a three-step process. At first, the ions transferred from the solution to the exterior surface and evenly distributed on ZVI@GRM surface. After that, the Pb(II) and Cr(VI) migrated from the surface to interior pores according to pore diffusion. Finally, the heavy metal ions were absorbed at the active site on the interior surface of ZVI@GRM and the adsorption process reached equilibrium.

In order to further explore the removal mechanism of Pb(II) and Cr(VI), the properties of the ZVI@GRM before and after adsorption were characterized. The elemental distribution of ZVI@GRM by using SEM-EDS was shown in Fig. 9a. The result showed that ZVI@GRM before reaction mainly consisted of O, C, Fe, Si and Al. The new peaks of Pb and Cr were appeared after reacting, respectively. Meanwhile, the Fe content in ZVI@GRM after reaction with Pb(II) and Cr(VI) were reduced. This could be explained that Pb and Cr were adsorbed on the material and Fe^0 participated in the reaction of Pb(II) and Cr(VI).

The XRD images of ZVI@GRM are shown in Fig. 9b. After the reaction, the typical diffraction peak of Fe^0 (2θ at 44.64°, 65.166°) disappeared, and the peaks of some new products Pb^0 (2θ at 42.53°), $PbO{\cdot}xH_2O$ (2θ at 32.72°), $FeCr_2O_4$ (2θ at 30.33° and 35.14°), Cr_2O_3 (2θ at 36.28° and 54.74°) began to appear.[36] This result demonstrated that Pb(II) and Cr(VI) were adsorbed and precipitated onto surface of ZVI@GRM. These products are mainly derived from the redox reaction of Fe^0 as a reductant directly or indirectly with Pb(II) and Cr(VI).

Table 5 Comparison of maximum removal capacity of Pb(II) and Cr(VI) by various adsorbents

Adsorbents	Heavy metal	q_m (mg g^{-1})	Reference
ZVI@GRM	Pb(II)	188.67	This study
Kaolinite supported NZVI	Pb(II)	48	31
Activated carbon supported NZVI	Pb(II)	59.35	43
Fly ash supported ZVI	Pb(II)	78.13	46
Sepiolite supported NZVI	Pb(II)	44.05	36
Magnetic biochar supported NZVI	Pb(II)	187.7	47
ZVI@GRM	Cr(VI)	51.55	This study
Biochar-supported NZVI	Cr(VI)	26.6	48
Fly ash supported ZVI	Cr(VI)	15.70	46
Modified biochar supported NZVI	Cr(VI)	17.8	33
Sepiolite supported NZVI	Cr(VI)	43.86	36
Humus-supported NZVI	Cr(VI)	40.40	38

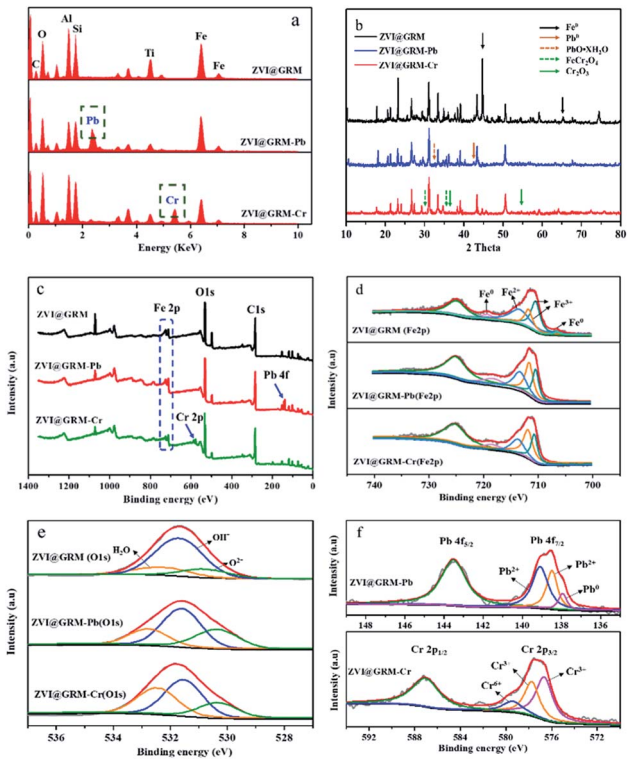

Fig. 9 The EDS survey (a), XRD pattern (b), XPS spectra of survey scan (c), Fe 2p region (d), O 1s region (e), Pb 4f and Cr 2p region (f) of ZVI@GRM before and after reaction.

Further characterization of ZVI@GRM was done by using the XPS technique to investigate the surface elemental composition and valence state. The typical XPS survey spectrum (Fig. 9c) shown that the ZVI@GRM surface was mainly composed of C, O and Fe, which corresponds to the results of SEM-EDS and XRD analysis. The intense C 1s signal was mainly derived from the biochar formed by the pyrolysis of maize straw, C and Fe^0 can form an Fe–C micro-electrolysis system to promote the removal of heavy metal ions. Furthermore, the XPS survey spectrum of ZVI@GRM after Pb(II) and Cr(VI) removal shown an obvious occurrence of Pb (139.08 eV) and Cr (577.08 eV) spectra. The result further indicated that Pb and Cr were immobilized on to ZVI@GRM. The detailed XPS surveys of Fe 2p, O 1s, Pb 4f and Cr 2p in ZVI@GRM and after removal are presented in Fig. 9d–f. As shown in Fig. 9d, the Fe 2p XPS survey spectrum has two peaks at corresponding to the binding energy of Fe $2p_{3/2}$ (711.78 eV) and Fe $2p_{1/2}$ (724.86 eV) of oxidized iron. The decomposed peaks located at near 710.47 and 711.78 eV were assigned Fe $2p_{3/2}$ of Fe^{3+}, the peaks at 713.4 eV was correspond to Fe^{2+}, which were existed in the form of FeOOH, Fe_2O_3 and Fe_3O_4, respectively.[49] Moreover, a small peak at 706.51 eV was also observed on ZVI@GRM corresponding to the peak of Fe^0 (Fe $2p_{3/2}$).[43] After the reaction, the peak of Fe^0 disappeared and the peak area corresponding to Fe^{3+} increased. This indicated that Fe^0 reacted with Pb(II) and Cr(VI), and the ions may co-precipitate with iron oxides/hydroxides. The spectra of O 1s resolved into three peaks at 530.57, 531.71 and 532.48 eV, which represented the binding energies of O^{2-}, OH^- and physically or chemically adsorbed water (H_2O), respectively. These results indicated that the ZVI@GRM surface was mainly composed of iron hydroxides or hydroxyl oxides, similar to the previous studies.[36] In Fig. 9e, the peaks position and area changed significantly were mainly due to the oxygen-containing functional groups on the surface of ZVI@GRM participated in the removal progress with the formation of oxides and hydroxides such as Cr $(OH)_3/Cr_2O_3$ and Pb $(OH)_2$. The spectra of Pb 4f and Cr 2p on the ZVI@GRM after Pb(II) and Cr(VI) removal were investigated in Fig. 9f. The observed peaks at 139.09 and 138.48 eV correspond to Pb(II) existed as Pb $(OH)_2$ or PbO and the peak at 137.94 eV was assigned to Pb^0 by the reduction of Fe^0 with Pb(II) on the ZVI@GRM surface.[43,49] The Cr $2p_{3/2}$ spectra could be divided into three peaks at 579.40, 577.74 and 576.66 eV. The peaks at 577.74 and 576.66 eV correspond to Cr(III) derived from Cr_2O_3 and Cr $(OH)_3$ due to the reduction by Fe^0 with Cr(VI), meanwhile the peak observed at 579.40 eV was attributed to Cr(VI) adsorbed on ZVI@GRM.[49] These results demonstrated that the adsorption and reduction of Pb(II) and Cr(VI) occurred simultaneously on ZVI @GRM.

In summary, based on the previous results analysis, the possible mechanism for removal Pb(II) and Cr(VI) by ZVI@GRM is shown in Fig. 10. Pb(II) and Cr(VI) was reduced by ZVI and

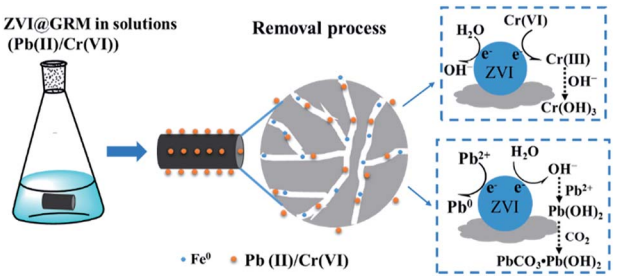

Fig. 10 Schematic of Pb(II) and Cr(VI) removal process by ZVI@GRM from aqueous solution.

coprecipitated or precipitated on the surface of ZVI@GRM. The Pb(II) quickly migrated to the surface and the part of adsorbed Pb(II) was directly reduced to Pb^0 by ZVI. In addition, the Pb $(OH)_2$ precipitated was formed by the reaction between Pb(II) in solution with OH^- produced from the H_2O reduced by the supported ZVI. The $PbCO_3 \cdot Pb(OH)_2$ was formed through a portion of Pb $(OH)_2$ interact with CO_2 dissolved in the solution. Cr(VI) was reduced to Cr(III) and simultaneously immobilized by precipitation as Cr $(OH)_3/Cr_2O_3$ or Cr(III)/Fe^{3+} hydroxides formed with the iron hydroxide/iron oxide on the surface. However, these hydroxides covering the ZVI@GRM surface may hinder the electron transfer from Fe^0 to the surface and cause a negative impact on the redox process, resulting in reduced Cr(VI) removal, especially at high concentrations.[38]

Besides, a lot of microscopic galvanic couples could be produced between the ZVI and carbon material in the reaction system. In the galvanic cell, electrons migrated from the anode (ZVI) to the cathode (C), while generating Fe(II) or atomic/molecular hydrogen (H/H_2) simultaneously, resulting in reducing the concentration of Pb(II) and Cr(VI).[33]

4. Conclusions

In this study, ZVI@GRM was prepared by using three raw materials (red mud, bentonite and maize straw) and was used to removal Pb(II) and Cr(VI) from aqueous solution. ZVI was synthesized and embedded in the granular porous adsorbent by direct reduction of iron oxide in red mud. Compared with the liquid phase method to prepare ZVI, the carbothermal reduction method is cheap and convenient to operate. Meanwhile, the raw materials are solid waste, and the reasonable use can make waste resources. The removal experiment results shown that ZVI@GRM has a higher removal capacity for Pb(II) and Cr(VI) and the removal mechanism was a three-step process, including adsorption and reduction of Pb(II) and Cr(VI). Pb(II) was adsorbed and then partly reduced to Pb^0 and formed Pb $(OH)_2$, $PbCO_3$ or $PbCO_3 \cdot Pb(OH)_2$ precipitated on the surface or internal layers by ZVI@GRM. Cr(VI) was adsorbed and then reduced to Cr(III) as Cr $(OH)_3$ or Cr^{3+}–Fe^{3+} hydroxides. Maximum removal capacity was calculated to be 188.67 mg g^{-1} of Pb(II) and 51.55 mg g^{-1} of Cr(VI). The results indicated that ZVI@GRM shows great potential for remediation heavy metals in wastewater.

Conflicts of interest

The authors declare no competing financial interest.

Acknowledgements

The authors acknowledge the support of the Zhaoqing Science and Technology Project (2018N006) and the Key Project of the Joint Fund Between the State Fund Committee and Shandong Province (U1806210) and National Key R&D Program of China (2017YFB0310801).

References

1 X. Kong, M. Li, S. Xue, W. Hartley, C. Chen, C. Wu, X. Li and Y. Li, Acid transformation of bauxite residue: Conversion of its alkaline characteristics, *J. Hazard. Mater.*, 2016, **324**, 382.
2 X. Zhu, W. Li and X. Guan, An active dealkalization of red mud with roasting and water leaching, *J. Hazard. Mater.*, 2015, **286**, 85–91.
3 T. Kinnarinen, L. Holliday and A. Häkkinen, Dissolution of sodium, aluminum and caustic compounds from bauxite residues, *Miner. Eng.*, 2015, **79**, 143–151.
4 Y. Liu and R. Naidu, Hidden values in bauxite residue (red mud): Recovery of metals, *Waste Manag.*, 2014, **34**, 2662–2673.
5 S. Xue, F. Zhu, X. Kong, C. Wu, L. Huang, N. Huang and W. Hartley, A review of the characterization and revegetation of bauxite residues (Red mud), *Environ. Sci. Pollut. Res.*, 2016, **23**, 1120–1132.
6 S. Yang, Y. Zhang, J. Yu, T. Huang, T. Qi, P. K. Chu and Q. Lei, Multi-functional honeycomb ceramic materials produced from bauxite residues, *Mater. Des.*, 2014, **59**, 333–338.
7 Y. Pontikes and G. N. Angelopoulos, Bauxite residue in cement and cementitious applications: Current status and a possible way forward, *Resour., Conserv. Recycl.*, 2013, **73**, 53–63.
8 Y. Hua, K. V. Heal and W. Friesl-Hanl, The use of red mud as an immobiliser for metal/metalloid-contaminated soil: A review, *J. Hazard. Mater.*, 2016, **325**, 17.
9 M. Samouhos, M. Taxiarchou, P. E. Tsakiridis and K. Potiriadis, Greek "red mud" residue: A study of microwave reductive roasting followed by magnetic separation for a metallic iron recovery process, *J. Hazard. Mater.*, 2013, **254–255**, 193–205.
10 C. R. Borra, B. Blanpain, Y. Pontikes, K. Binnemans and T. V. Gerven, Smelting of Bauxite Residue (Red Mud) in View of Iron and Selective Rare Earths Recovery, *Journal of Sustainable Metallurgy*, 2016, **2**, 28–37.
11 Y. Jie, X. Cong, P. Zhang, E. Hoffmann, G. Zeng, L. Yang, F. Wei, W. Yan and H. Zhang, Interaction between phosphate and acid-activated neutralized red mud during adsorption process, *Appl. Surf. Sci.*, 2015, **356**, 128–134.
12 Z. Qi, W. An, C. Wu, W. Li, A. Fu, R. Xiao, H. Chen and S. Xue, Red mud-modified biochar reduces soil arsenic availability and changes bacterial composition, *Environ. Chem. Lett.*, 2017, 1–8.

13 Q. Yue, Y. Zhao, L. Qian, W. Li, B. Gao, S. Han, Y. Qi and Y. Hui, Research on the characteristics of red mud granular adsorbents (RMGA) for phosphate removal, *J. Hazard. Mater.*, 2010, **176**, 741–748.

14 S. Zhang, C. Liu, Z. Luan, X. Peng, H. Ren and J. Wang, Arsenate removal from aqueous solutions using modified red mud, *J. Hazard. Mater.*, 2008, **152**, 486–492.

15 T. Ali, D. Nadide, A. Gulsin and C. Yunus, Removal of fluoride from water by using granular red mud: Batch and column studies, *J. Hazard. Mater.*, 2009, **164**, 271–278.

16 N. J. Ward, L. A. Sullivan and R. T. Bush, Sulfide oxidation and acidification of acid sulfate soil materials treated with $CaCO_3$ and seawater-neutralised bauxite refinery residue, *Soil Res.*, 2002, **40**, 1057–1067.

17 X. Qi, H. Wang, C. Huang, L. Zhang, J. Zhang, B. Xu, F. Li and J. T. A. Junior, Analysis of bauxite residue components responsible for copper removal and related reaction products, *Chemosphere*, 2018, 209–217.

18 K. Binnemans, P. T. Jones, B. Blanpain, T. V. Gerven and Y. Pontikes, Towards zero-waste valorisation of rare-earth-containing industrial process residues: a critical review, *J. Cleaner Prod.*, 2015, **99**, 17–38.

19 C. R. Borra, B. Blanpain, Y. Pontikes, K. Binnemans and T. Van Gerven, Recovery of Rare Earths and Other Valuable Metals from Bauxite Residue (Red Mud): A Review, *Journal of Sustainable Metallurgy*, 2016, **2**, 365–386.

20 C. Cardenia, E. Balomenos and D. Panias, Iron Recovery from Bauxite Residue Through Reductive Roasting and Wet Magnetic Separation, *Journal of Sustainable Metallurgy*, 2019, **5**, 9–19.

21 S. Rai, M. T. Nimje, M. J. Chaddha, S. Modak, K. R. Rao and A. Agnihotri, Recovery of iron from bauxite residue using advanced separation techniques, *Miner. Eng.*, 2019, **134**, 222–231.

22 C. R. Borra, B. Blanpain, Y. Pontikes, K. Binnemans and T. Van Gerven, Smelting of Bauxite Residue (Red Mud) in View of Iron and Selective Rare Earths Recovery, *Journal of Sustainable Metallurgy*, 2016, **2**, 28–37.

23 Z. Li, L. Wang, J. Meng, X. Liu, J. Xu, F. Wang and P. Brookes, Zeolite-supported nanoscale zero-valent iron: New findings on simultaneous adsorption of Cd(II), Pb(II), and As(III) in aqueous solution and soil, *J. Hazard. Mater.*, 2017, **344**, 1–11.

24 F. Fu, D. D. Dionysiou and L. Hong, The use of zero-valent iron for groundwater remediation and wastewater treatment: A review, *J. Hazard. Mater.*, 2014, **267**, 194–205.

25 J. Liu, Y. Wang, F. Yi, T. Mwamulima, S. Song and C. Peng, Removal of crystal violet and methylene blue from aqueous solutions using the fly ash-based adsorbent material-supported zero-valent iron, *J. Mol. Liq.*, 2018, **250**, 468–476.

26 A. Mossmann, G. L. Dotto, D. Hotza, S. L. Jahn and E. L. Foletto, Preparation of polyethylene–supported zero–valent iron buoyant catalyst and its performance for Ponceau 4R decolorization by photo–Fenton process, *J. Environ. Chem. Eng.*, 2019, **7**, 102963.

27 Q. Yue, Y. Zhao, Q. Li, W. Li, B. Gao, S. Han, Y. Qi and H. Yu, Research on the characteristics of red mud granular adsorbents (RMGA) for phosphate removal, *J. Hazard. Mater.*, 2010, **176**, 741.

28 I. Hussain, M. Li, Y. Zhang, Y. Li, S. Huang, X. Du, G. Liu, W. Hayat and N. Anwar, Insights into the mechanism of persulfate activation with nZVI/BC nanocomposite for the degradation of nonylphenol, *Chem. Eng. J.*, 2017, **311**, 163–172.

29 Z. Cheng, Z. Gao, W. Ma, Q. Sun, B. Wang and X. Wang, Preparation of magnetic Fe_3O_4 particles modified sawdust as the adsorbent to remove strontium ions, *Chem. Eng. J.*, 2012, **209**, 451–457.

30 E. Petala, K. Dimos, A. Douvalis, T. Bakas, J. Tucek, R. Zbořil and M. A. Karakassides, Nanoscale zero-valent iron supported on mesoporous silica: Characterization and reactivity for Cr(VI) removal from aqueous solution, *J. Hazard. Mater.*, 2013, **261**, 295–306.

31 X. Zhang, S. Lin, Z. Chen, M. Megharaj and R. Naidu, Kaolinite-supported nanoscale zero-valent iron for removal of Pb^{2+} from aqueous solution: Reactivity, characterization and mechanism, *Water Res.*, 2011, **45**, 3481–3488.

32 D. Ouyang, J. Yan, L. Qian, Y. Chen, L. Han, A. Su, W. Zhang, H. Ni and M. Chen, Degradation of 1,4-dioxane by biochar supported nano magnetite particles activating persulfate, *Chemosphere*, 2017, **184**, 609–617.

33 H. Dong, J. Deng, Y. Xie, C. Zhang, Z. Jiang, Y. Cheng, K. Hou and G. Zeng, Stabilization of nanoscale zero-valent iron (nZVI) with modified biochar for Cr (VI) removal from aqueous solution, *J. Hazard. Mater.*, 2017, **332**, 79–86.

34 Z.-H. Diao, J.-J. Du, D. Jiang, L.-J. Kong, W.-Y. Huo, C.-M. Liu, Q.-H. Wu and X.-R. Xu, Insights into the simultaneous removal of Cr^{6+} and Pb^{2+} by a novel sewage sludge-derived biochar immobilized nanoscale zero valent iron: Coexistence effect and mechanism, *Sci. Total Environ.*, 2018, **642**, 505–515.

35 Z. Dongsheng, G. Wenqiang, C. Guozhang, L. Shuai, J. Weizhou and L. Youzhi, Removal of heavy metal lead (II) using nanoscale zero-valent iron with different preservation methods, *Adv. Powder Technol.*, 2019, **30**, 581–589.

36 R. Fu, Y. Yang, Z. Xu, X. Zhang, X. Guo and D. Bi, The removal of chromium (VI) and lead (II) from groundwater using sepiolite-supported nanoscale zero-valent iron (S-NZVI), *Chemosphere*, 2015, **138**, 726–734.

37 C. Fan, K. Li, J. Li, D. Ying, Y. Wang and J. Jia, Comparative and competitive adsorption of Pb (II) and Cu (II) using tetraethylenepentamine modified chitosan/$CoFe_2O_4$ particles, *J. Hazard. Mater.*, 2017, **326**, 211–220.

38 R. Fu, X. Zhang, Z. Xu, X. Guo, D. Bi and W. Zhang, Fast and highly efficient removal of chromium (VI) using humus-supported nanoscale zero-valent iron: Influencing factors, kinetics and mechanism, *Sep. Purif. Technol.*, 2017, **174**, 362–371.

39 Y. Bagbi, A. Sarswat, S. Tiwari, D. Mohan, A. Pandey and P. R. Solanki, Synthesis of l-cysteine stabilized zero-valent iron (nZVI) nanoparticles for lead remediation from water, *Environmental Nanotechnology, Monitoring & Management*, 2017, **7**, 34–45.

40 A. Tor, Y. Cengeloglu, M. E. Aydin and M. Ersoz, Removal of phenol from aqueous phase by using neutralized red mud, *J. Colloid Interface Sci.*, 2006, **300**, 498–503.
41 A. Tor, N. Danaoglu, G. Arslan and Y. Cengeloglu, Removal of fluoride from water by using granular red mud: Batch and column studies, *J. Hazard. Mater.*, 2009, **164**, 271–278.
42 A. Mittal, J. Mittal, A. Malviya, D. Kaur and V. K. Gupta, Adsorption of hazardous dye crystal violet from wastewater by waste materials, *J. Colloid Interface Sci.*, 2010, **343**, 463–473.
43 X. Liu, D. Lai and Y. Wang, Performance of Pb(II) removal by an activated carbon supported nanoscale zero-valent iron composite at ultralow iron content, *J. Hazard. Mater.*, 2019, **361**, 37–48.
44 A. Z. El-Sonbati, I. M. El-Deen and M. A. El-Bindary, Molecular docking, potentiometric and thermodynamic studies of azo rhodanines, *J. Mol. Liq.*, 2016, **221**, 51–60.
45 A. R. Kul and H. Koyuncu, Adsorption of Pb(II) ions from aqueous solution by native and activated bentonite: Kinetic, equilibrium and thermodynamic study, *J. Hazard. Mater.*, 2010, **179**, 332–339.
46 J. Liu, T. Mwamulima, Y. Wang, Y. Fang, S. Song and C. Peng, Removal of Pb(II) and Cr(VI) from aqueous solutions using the fly ash-based adsorbent material-supported zero-valent iron, *J. Mol. Liq.*, 2017, 243.
47 Y.-d. Chen, S.-H. Ho, D. Wang, Z.-s. Wei, J.-S. Chang and N.-q. Ren, Lead removal by a magnetic biochar derived from persulfate-ZVI treated sludge together with one-pot pyrolysis, *Bioresour. Technol.*, 2018, **247**, 463–470.
48 L. Qian, W. Zhang, J. Yan, L. Han, Y. Chen, D. Ouyang and M. Chen, Nanoscale zero-valent iron supported by biochars produced at different temperatures: Synthesis mechanism and effect on Cr(VI) removal, *Environ. Pollut.*, 2017, **223**, 153–160.
49 Z. H. Diao, J. J. Du, D. Jiang, L. J. Kong, W. Y. Huo, C. M. Liu, Q. H. Wu and X. R. Xu, Insights into the simultaneous removal of Cr^{6+} and Pb^{2+} by a novel sewage sludge-derived biochar immobilized nanoscale zero valent iron: Coexistence effect and mechanism, *Sci. Total Environ.*, 2018, **642**, 505.